Evolutions of the seasonal anticyclonic circulation around the Qingdao cold water mass in the China marginal sea and its mechanism

Lin Lin[1, a,*], Hans von Storch[1], Yang Ding[2]

[1]Institute of Coastal Systems, Helmholtz Zentrum Hereon, Geesthacht, 21502, Germany
[2]Frontier Science Center for Deep Ocean Multispheres and Earth System (FDOMES) and Physical Oceanography Laboratory, Ocean University of China, Qingdao, 266100, China
[a]Currently at Max Planck Institute for Meteorology, Hamburg, 20146, Germany

Correspondence to: Lin Lin (lin.lin@mpimet.mpg.de).

Abstract. The circulation structure surrounding the Qingdao cold water mass in 2019 was investigated using three-dimensional ensembles of numerical simulations. This study reveals that a cold pool appears in early spring and reaches its peak in late May, and this pool is accompanied by local seasonal anticyclonic circulation. Momentum diagnostics reveal that vertical friction cannot be ignored because of the shallow topography and surface wind stress; as a result, the geostrophic balance is inapplicable in the Qingdao cold water mass region. Seasonal circulation mostly results from the balance of the pressure gradient, Coriolis, and vertical friction forces. The no-tide and no-wind numerical simulation results suggest that when the tidal forcing is turned off, unrealistically strong currents appear and are caused by the decrease in vertical friction in the no-tide simulation. Moreover, the direction of the eastern side of the anticyclonic circulation is reversed. Furthermore, the seasonal southwesterly monsoon contributes to the magnitude of the anticyclonic circulation, especially in the western portion of the anticyclonic circulation. Additionally, upwelling occurs vertically around the Qingdao cold water mass and is influenced by tidal and wind forcings. The wind forcing affects upwelling (especially in the western part), which can be explained by Ekman pumping; the tides contribute to upwelling in the eastern part by reshaping the thermocline and further changing the baroclinic pressure gradient force. Ensemble simulations are used, and the t-test reveal that 51.29% (89.68%) of points, difference between the control run and the ensemble experiments without tidal forcing (/without wind forcings) is statistically significant.

1. Introduction

The Qingdao cold water mass was first identified in 1959 and occurs in deep waters below 25 m in the southeastern offshore region of Qingdao during the spring season (the position of Qingdao and the position mentioned in this paper are shown in Fig. 1) (Ho et al. 1959). This cold water mass is an isolated cold pool characterized by low temperature (6.5–10.0°C), moderate salinity (31.5–32.5), and seasonal variation (Zheng and Zhang 1983). This cold water mass has a significant influence on aquaculture in China since it is situated near the Chinese coastline (cunyi Zhang 1986; Y. Zhang and Geng 1989; Zheng and Zhang 1983). The temperature, salinity, and circulation distribution of the Qingdao cold water mass play important roles in the ecosystem, such as in primary production (Q. Wei et al. 2019). Numerous researchers have conducted surveys on the origin and characteristics of the Qingdao cold water mass and reported that it forms in late April, peaks in May, and gradually moves eastward, with both the temperature and salinity increasing. After June, this cold water mass gradually disappears as it merges with the bottom layer of the Yellow Sea (Diao 2015; Yu et al. 2006; Q. Zhang, Yang, and Cheng 1994; Q. Zhang et al. 2004). Although the Qingdao cold water mass lifetime is relatively short, it is considered an independent water mass because of its unique patterns of both formation and evolution. On the basis of observational data, Zhang et al. (2002) analyzed the source and temperature–salinity characteristics of the Qingdao cold water mass, indicating that it formed in the local environment by the Bohai Sea coastal current bypassing the Shandong Peninsula. This cold water mass is characterized by low temperature, moderate salinity, and high dissolved oxygen. Zhang et al. (2004) analyzed the intensity variations in the Qingdao cold water mass. Their results suggest that it disappears gradually in June and July. However, some studies have reported the presence of the Qingdao cold water mass in August (J. Xia and Xiong 2013). Yu et al. (2005, 2006) analyzed the relationship between the Qingdao cold water mass and the Yellow Sea cold water mass and reported that in June, the Qingdao cold water mass was already on the edge of the Yellow Sea cold water mass; it was no longer a local independent water mass but rather a local cold center within the Yellow Sea cold water mass. Huang et al. (2019) used numerical simulations to reveal that the cold and moderate-salinity water in the offshore area between Qingdao and Shidao in the southwestern Yellow Sea was an early form of the Qingdao cold water mass. Additionally, the strong horizontal temperature gradient is the thermodynamic mechanism by which the Qingdao cold water mass forms (Zhang et al., 2016). On the basis of the previous studies mentioned above, conclusions have been drawn regarding the seasonal variations and origins of the Qingdao cold water mass. Previous work has demonstrated that a mesoscale anticyclone exists near the Qingdao coast, and its position is close to the Qingdao cold water mass (Huang, Chen, and Lin 2019; F. Zhang, Mao, and Leng 1987). However, it is unknown whether the formation of this anticyclonic circulation is related to the Qingdao cold water mass.

There are other cold water masses in the Bohai and Yellow Seas, the marginal seas along China, such as the cold pool in the Bohai Sea (Liu et al. 2003; Wan et al. 2004; Zhou et al. 2017), and the Yellow Sea cold water mass (Ho et al. 1959; Hur, Jacobs, and Teague 2000; H. Wei et al. 2010; Yuan et al. 2013). The special circulation structures around the Bohai cold water mass and Yellow Sea cold water mass have been well described in previous studies (Wang et al. 2014; C. Xia et al. 2006; Zhou et al. 2017; Zhu and Wu 2018), but the anticyclone current field analysis near the Qingdao cold water mass still needs to be investigated. In this work, we investigate the following questions: (1) Is the Qingdao cold water mass causing the local seasonal anticyclonic structure? Does such a seasonal anticyclonic circulation fit the geostrophic balance? (2) What factors influence the morphology, magnitude, and position of the seasonal anticyclonic circulation horizontally and vertically?

The paper is organized as follows. The model configuration and model design are described in Section 2. In this section, the concept and logic of ensemble simulations and the need to consider the internal variability (for the definition of internal variability, see Section 2.2) of the marginal sea are described. Section 3 shows the results of the ensemble mean of the control simulations with respect to the simulated temperature, salinity, circulation structure, and momentum balance in the Qingdao cold water mass. In Section 4, potential factors affecting the horizontal circulation pattern and the upwelling structures of the Qingdao cold water mass are discussed. Finally, conclusions are given in Section 5.

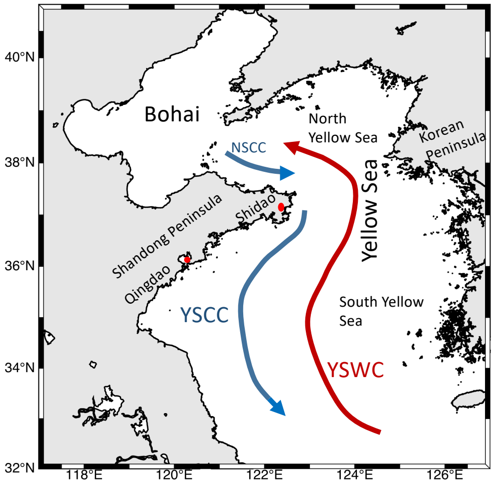

Figure 1. Maps of the Bohai Sea, Yellow Sea (North and South Yellow Seas), Shandong Peninsula, Korean Peninsula, Shidao, Qingdao, North Shandong Coastal Current (NSCC), and Yellow Sea Coastal Current (YSCC).

2. Methods and model

2.1 Model configuration

In this work, we used the three-dimensional unstructured grid finite volume coastal ocean model (FVCOM) (Chen, Liu, and Beardsley 2003; Chen, Beardsley, and Cowles 2006). The horizontal grid resolution is approximately 4 and 8 km in the Bohai and Yellow Seas, respectively. Vertically, the model comprises 30 sigma layers. The vertical and horizontal diffusion coefficients were calculated using the Mellor and Yamada level 2.5 (MY-2.5) turbulent closure model (Mellor and Yamada 1982) and the Smagorinsky eddy parameterization method, respectively. The model domain includes the Bohai and Yellow

Seas, ranging from 31.885°N–40.942°N and 117.572°E–126.915°E, respectively (Fig. 1 in Lin et al. (2023)). The open boundary across the Yellow Sea extends eastward from Qidong in China to the southern tip of the Korean Peninsula, and radiation boundary conditions were used. For the control run, the six-hourly surface forcing data utilized in this study are from the National Centers for Environmental Prediction (NCEP) Climate Forecast System Version 2 (CFSv2) data, featuring a global resolution of 0.2° × 0.2° (Saha et al. 2014). This dataset encompasses parameters such as sea surface temperature, cloud cover, air pressure, wind, specific humidity, evaporation, precipitation, and heat flux. The initial data of the model are introduced in the following ensemble experimental design section. The tidal elevation forcing comprises eight major tidal components ($\mathrm{M_2}$, $\mathrm{S_2}$, $\mathrm{N_2}$ $\mathrm{K_2}$, $\mathrm{K_1}$, $\mathrm{O_1}$, $\mathrm{P_1}$, and $\mathrm{Q_1}$) derived from the TPXO8 database (Egbert and Erofeeva 2002). The model-simulated elevation, temperature, salinity, and circulation patterns were validated by information in Huang et al. (2019) and Lin et al. (2022, 2023). This study focuses directly on the analysis and discussion of the Qingdao cold water mass.

2.2 Ensemble experimental design

An ensemble of control runs was first used to analyze the temperature, salinity, and velocity around the Qingdao cold water mass. Additionally, two further ensembles of model experiments were conducted. The first experiment was performed with tidal forcing turned off to examine the effect of tides on the Qingdao cold water mass, and the second experiment was performed with wind forcing turned off (zero wind stress) to test the effect of the wind. The model output interval was 3 h. A more thorough description of the ensemble simulation configuration can be found in Lin et al. (2022).

Ensemble simulations were conducted for the control run, no-tide run, and no-wind run. Each ensemble simulation comprises four numerical simulation members. In each ensemble, the initial conditions of the four simulations were taken from Nov. 1st of the 9th year, Jan. 1st of the 10th year, Mar. 1st of the 10th year, and Nov. 1st of the 10th year of the separate 10-year climatological simulation. Note that an independent 10-year simulation was conducted to generate slightly different but generally consistent initial conditions for the ensemble simulation. The model starting time of the 10-year climatological simulation was Nov. 1st, 2008, and the model ending time was Nov. 1st, 2018. The climatological forcing for the climatological run was a smooth annual cycle without interannual variations based on National Centers for Environmental Prediction (NCEP) Climate Forecast System Version 2 (CFSv2) data. For the control, no-tide run, and no-wind run, the results for 2019 were used for further analysis. The model ending dates of the control run, no-tide, and no-wind runs were December 31st, 2019.

The motivation for using ensemble simulations is based on the observation (Lin et al. 2022; 2023; Penduff et al. 2019) that deviations form within the ensemble members if the ensemble simulations are conducted with the same model configuration except for slight perturbations in the initial conditions. In other words, if only one numerical simulation exists, the model output will be a mix of "signal" (external forcing) and random effects, which refer to variation among the ensemble means. The randomness reflects the internal variability. Some spatial features are not repeatable in other ensemble members, even though the model configurations are the same. Averaging across ensemble simulations efficiently reduces the impacts of randomness. Therefore, in Sections 3 and 4, the ensemble means were further analyzed. An ensemble simulation with slightly different initial conditions is an approach to analyzing ocean internal variability. Internal variability is defined as the part that cannot be linked directly to the external forcing but is caused by unforced variability generated within a system. The unforced variability is unprovoked and chaotic. Since this paper focuses on the external forcing imprint on the seasonal anticyclonic circulation around the Qingdao cold water mass, more details about the concept of internal variability can be found in previous studies (Tang, von Storch, and Chen 2020; Lin et al. 2023). For the ensemble simulation configuration in this study, the tradition of generating an ensemble simulation with slightly different initial conditions was adopted (Penduff et al. 2019). The deviations existing between ensemble members due to randomness necessitate testing whether the differences between the ensemble means of the control run and the no-tide run (/no-wind run) may be caused by external forcings (tidal or wind forcings) or randomness. A proper way to do so is hypothesis testing with the null hypothesis: “external forcing has no effect”. If this null hypothesis is rejected with a sufficiently small risk, then a valid conclusion is that an external factor has an effect and plays an active role. Here, a t test was performed for the ensemble monthly mean for May.

3. Results

3.1 Temperature and Salinity of the Qingdao Cold Water Mass

The temperature distribution at a depth of 25 m around the Qingdao cold water mass is shown in Fig. 2a–c. In March, the cold water carried by the Bohai coastal current approached the area around the Shandong Peninsula, gradually evolving to become the Qingdao cold water mass. However, the isotherms did not close, and the Qingdao cold water mass structure did not form at this time (Fig. A1). In April, a low-temperature tongue enveloped by an 8°C isotherm occurs north of 35°45′N and east of 121°45′E, accompanied by a horizontal temperature gradient. During this period, the high-temperature water transported by the northwest path of the Yellow Sea warm current remained in the western region of the South Yellow Sea, forming an apparent oceanfront with the Qingdao cold water mass (Fig. 2a). In May, the location of the cold water mass center does not change at a depth of 25 m (Fig. 2b). Combined with the salinity results shown in Fig. 2d–f, it is clear that the temperature and salinity are relatively low around the Shandong Peninsula. Moderately saline water intrudes toward the south, and the intrusion direction is northeast–southwest, which is consistent with previous research results (Diao 2015). The low-temperature and moderate-salinity water tongue along the northeast of the Shandong Peninsula merges with the ambient warm water left by the Yellow Sea cold water mass beginning in winter. In June (Fig. 2c), the temperature increases as solar radiation increases, accelerating the merging of warm and cold water and causing the Qingdao cold water mass to disappear. At this time, fast heating on the ocean surface induces strong and rapid stratification, sealing the cold water below the thermoclines. The vertical mixing due to wind disturbance or upwelling is not strong enough to homogenize the water column, resulting in the maintenance of a near-bottom cold water mass. In summary, the Qingdao cold water mass starts to merge in April, continues to develop in May, is accompanied by a strong horizontal temperature gradient, and disappears in June. The cold water mass center is at 122.20°–122.40°E, 36°–36.15°N, and the shape of the cold water mass has a northeast–southwest orientation.

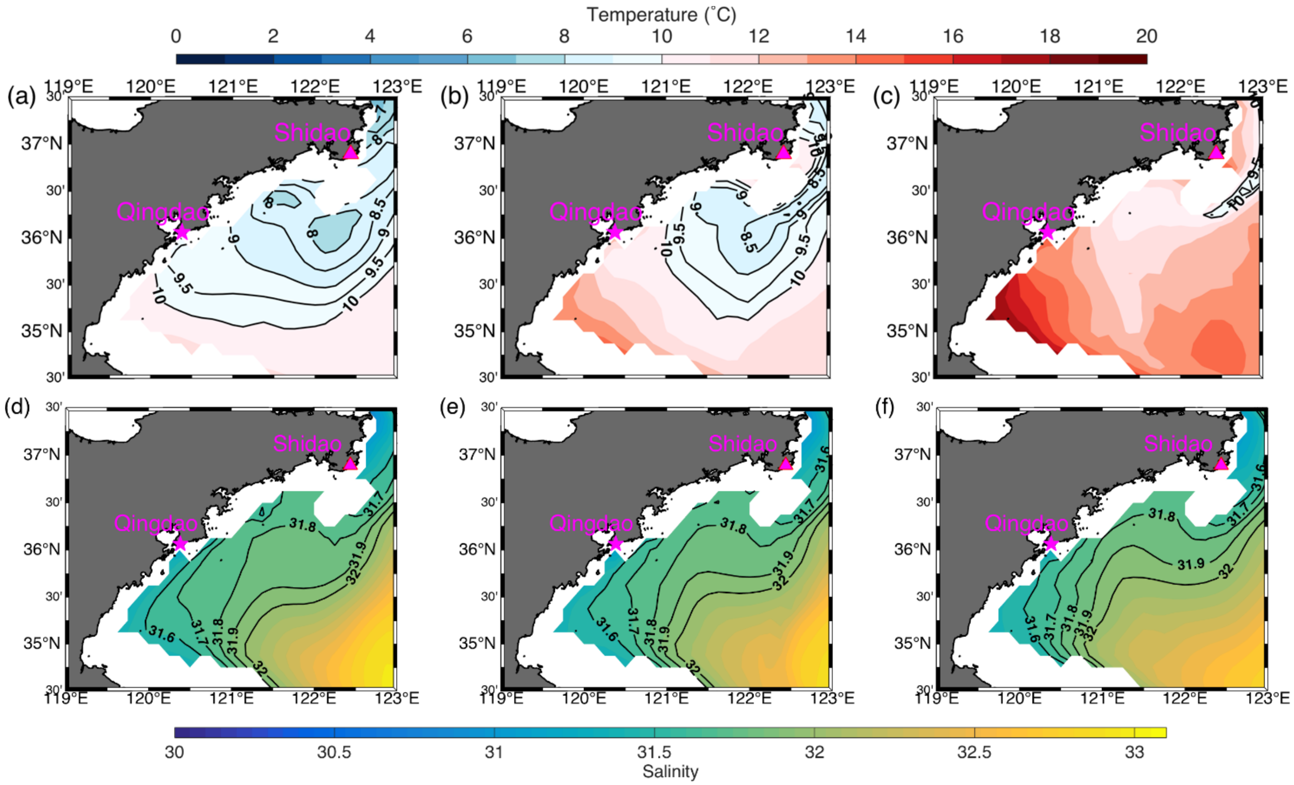

Figure 2. Monthly mean temperature and salinity evolution of the Qingdao cold water mass from April to June at a depth of 25 m according to the ensemble mean of the control runs. Figs. 2a, b, and c show the temperature distributions of the peaks of the Qingdao cold water mass (in April), the gradual disappearance (in May), and the complete disappearance (in June), respectively. Figs. 2d–f are the same as Figs. 2a–c but for salinity. To clearly present the temperature distribution, the isotherms between 8℃ and 10℃ are marked with 0.5℃ intervals.

3.2 Circulation Pattern

A seasonal anticyclonic structure exists near the Qingdao cold water mass. Fig. 3 shows the circulation at a depth of 25 m from April to June. In April, the seasonal anticyclonic structure is not closed. In May, a southwesterly monsoon prevails near the Shandong Peninsula, and a northward current can be seen along the Shandong Peninsula coastline, meeting the southward current between 122°E and 123°E. In May, the seasonal anticyclonic structure nearly closes, and the northeastward flow on the west side of the anticyclonic structure is stronger than the southwestward current on the east side. The center position of the seasonal anticyclonic circulation is 122.35°-122.45°E, 35.45-°35.55°N, and the velocity at the center of the anticyclonic circulation is very slow. In June, the seasonal anticyclonic circulation disappears when the southward current is strengthened. The above simulation results are consistent with those of previous studies (Xu and Zhao 1999; F. Zhang, Mao, and Leng 1987). As the water depth is shallow in the western portion of the anticyclonic circulation and the dominant southeasterly monsoon, the current velocities in the western part of the anticyclonic circulation are stronger than those in the eastern part.

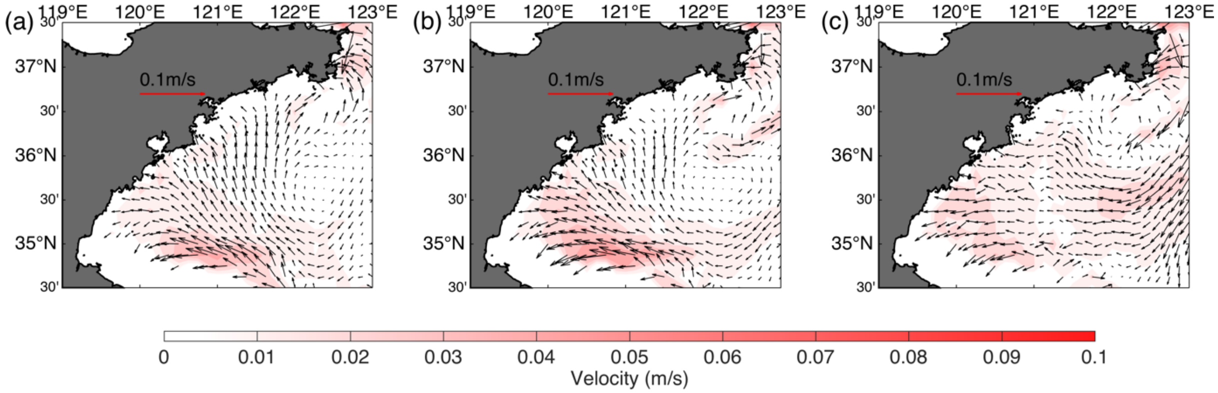

Figure 3. Horizontal circulation distributions around the Qingdao cold water mass (25 m layer) in (a) April, (b) May, and (c) June.

The circulation patterns at 25, 30, 35, and 40 m are shown in Fig. 4. The anticyclonic structure can still be observed at depths of 25 and 30 m. However, at the 35-m layer, the anticyclonic circulation does not close, as the current in the eastern part becomes weaker than that at a 25-m depth. At depths exceeding 35 m, the anticyclonic structure no longer exists. The patterns of the circulation structures in different layers are different, reflecting the baroclinic pressure gradient features of the current fields. The unique seasonal anticyclonic circulation structure hinders horizontal heat transfer, which could serve as a dynamic mechanism for the formation of the Qingdao cold water mass (Huang, Chen, and Lin 2019).

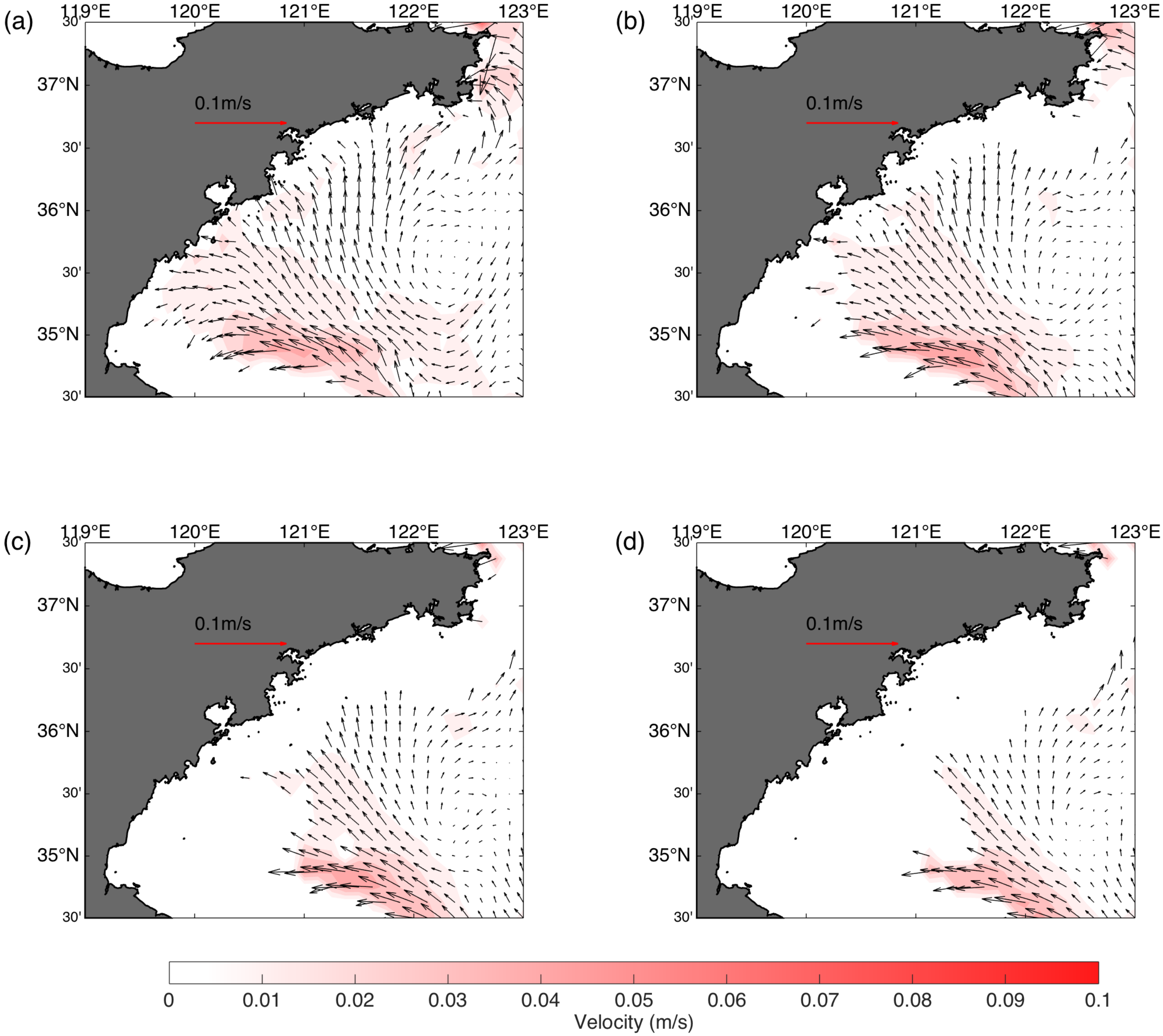

Figure 4. Circulation structure of the Qingdao cold water mass in May at depths of (a) 25, (b) 30, (c) 35, and (d) 40 m.

3.3 Momentum Balance

$$\frac{\partial u}{\partial t} = fv - \left(u\frac{\partial u}{\partial x} + v\frac{\partial u}{\partial y}\right) - w\frac{\partial u}{\partial z} - g\frac{\partial \zeta}{\partial x} - \frac{1}{\rho}\frac{\partial}{\partial x}\int_z^{\zeta}\rho g dz + \frac{\partial}{\partial z}\left(K_m\frac{\partial u}{\partial z}\right) + F_u \qquad (1)$$

$$\frac{\partial v}{\partial t} = -fu - \left(u\frac{\partial v}{\partial x} + v\frac{\partial v}{\partial y}\right) - w\frac{\partial v}{\partial z} - g\frac{\partial \zeta}{\partial y} - \frac{1}{\rho}\frac{\partial}{\partial y}\int_z^{\zeta}\rho g dz + \frac{\partial}{\partial z}\left(K_m\frac{\partial v}{\partial z}\right) + F_v \qquad (2)$$

$$\frac{\partial w}{\partial t} = -\left(u\frac{\partial w}{\partial x} + v\frac{\partial w}{\partial y}\right) - w\frac{\partial w}{\partial z} - \frac{\rho g}{\rho_0} + \frac{\partial}{\partial z}\left(K_m\frac{\partial w}{\partial z}\right) + F_w \qquad (3)$$

To show the general pattern of the fundamental forces around the Qingdao cold water mass anticyclonic circulation region, a momentum balance diagnostic was conducted (see Equations (1) – (3)). Taking the zonal direction as an example (Equation (1)), the total pressure gradient term is $-g\frac{\partial \zeta}{\partial x} - \frac{1}{\rho}\frac{\partial}{\partial x}\int_z^\zeta \rho g dz$, which comprises the barotropic pressure gradient force $-g\frac{\partial \zeta}{\partial x}$ induced by sea level and the baroclinic pressure gradient force $-\frac{1}{\rho}\frac{\partial}{\partial x}\int_z^\zeta \rho g dz$ induced by density; the Coriolis force fv; the vertical friction term $\frac{\partial}{\partial z}\left(K_m\frac{\partial u}{\partial z}\right)$; the local velocity time variation term $\frac{\partial u}{\partial t}$; the horizontal advection term $-(u\frac{\partial u}{\partial x} + v\frac{\partial u}{\partial y})$; the vertical advection term $-w\frac{\partial u}{\partial z}$; and the horizontal friction term F_u.

In the 25-m and 40-m (Fig. 5) layers, the terms for the barotropic pressure gradient, baroclinic pressure gradient, Coriolis force, and vertical friction are dominant, and the other terms are far smaller. The barotropic gradient force exceeds the baroclinic pressure gradient force and is balanced by the joint effects of the opposing baroclinic pressure gradient force, Coriolis force, and vertical friction force (the sum of the barotropic gradient force, baroclinic pressure gradient force, Coriolis force, and vertical friction force is shown in Fig. A2). The vertical friction is induced by wind stress from the surface layer (Fig. A3) and bottom friction from the bottom layer. In May, the southwesterly wind stress (Fig. A3) contributes to the northward current. Since the depth around the Qingdao cold water mass is relatively shallow, the friction caused by the tidal current and topography extends from the bottom layer to the middle layer, connecting with the wind stress from the surface layer, especially on the western side. Because there is vertical friction, a geostrophic balance no longer exists, especially in areas close to the coast. This issue is addressed in Section 3.5.

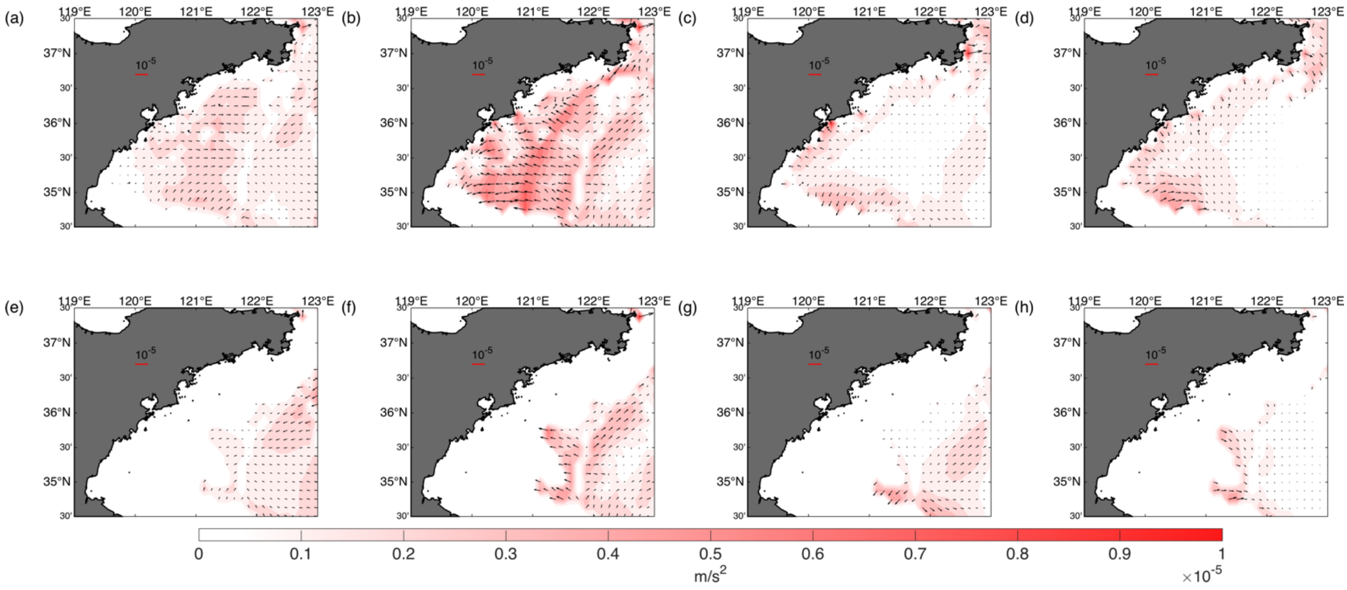

Figure 5. Horizontal distributions of momentum terms (monthly mean for May) at depths of (a–d) 25 and (e–h) 40 m: (a, e) Coriolis force ($fv\vec{i} - fu\vec{j}$), (b, f) barotropic pressure gradient force ($-g\frac{\partial \zeta}{\partial x}\vec{i} - g\frac{\partial \zeta}{\partial y}\vec{j}$), (c, g) baroclinic pressure gradient force ($-\frac{1}{\rho}\frac{\partial}{\partial x}\int_z^{\zeta}\rho g dz\,\vec{i} - \frac{1}{\rho}\frac{\partial}{\partial y}\int_z^{\zeta}\rho g dz$), and (d, h) vertical friction force ($F_u\vec{i} + F_v\vec{j}$). The color represents the magnitude of the momentum term.

3.4 Relation Between the Seasonal Anticyclone Circulation Pattern and the Qingdao Cold Water Mass

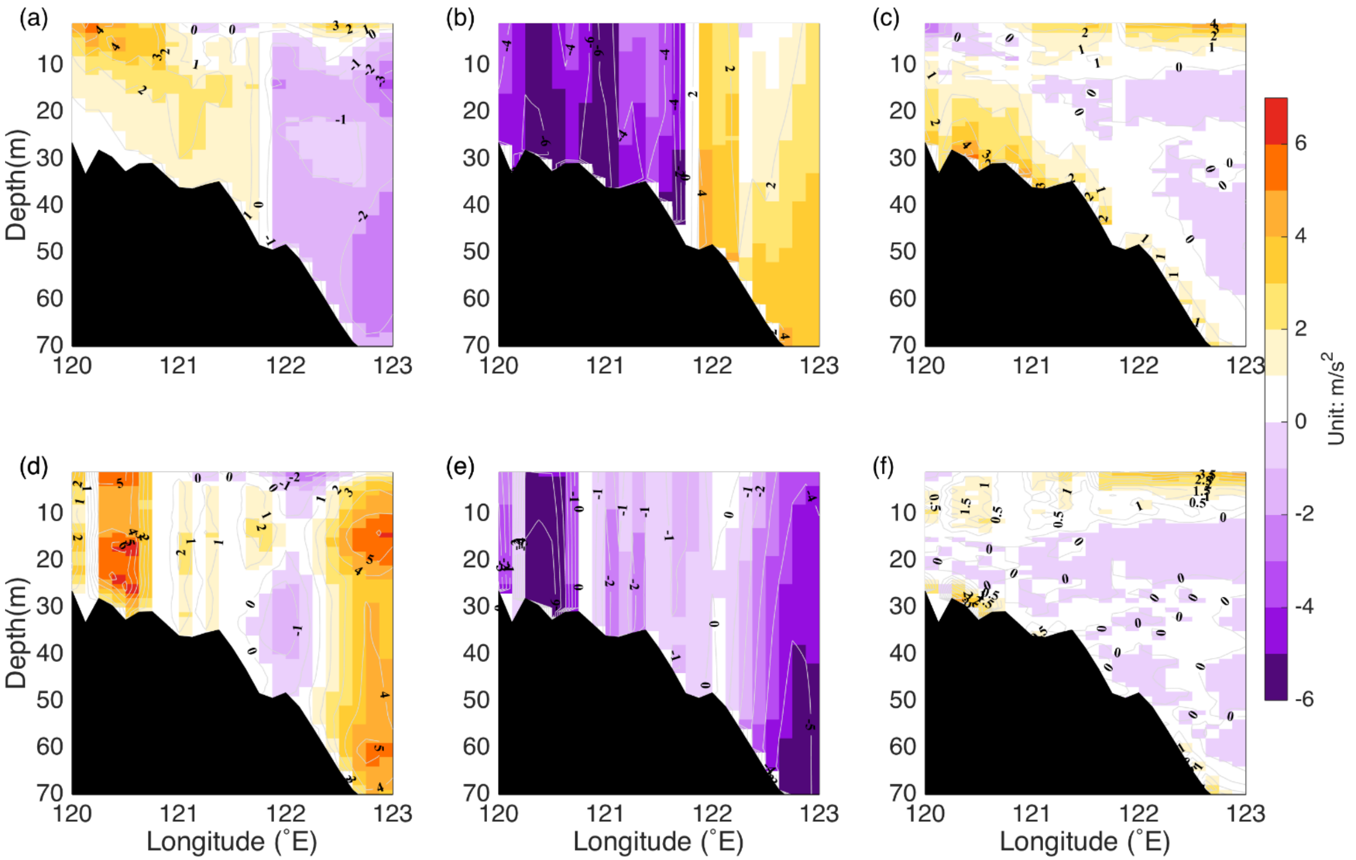

Figure 6. Vertical distribution of zonal momentum terms along the 35.5°N profile of the (a, b, c) control run and the (d, e, f) no-tide experiment. (a, d) Coriolis force fv, (b, e) total pressure gradient force $-g\frac{\partial \zeta}{\partial x} - \frac{1}{\rho}\frac{\partial}{\partial x}\int_z^{\zeta}\rho g dz$, and (c, f) vertical friction force F_u. The magnitude of the momentum terms has a time of 10^6 for visualization. A positive value represents the northward direction.

To further analyze the seasonal anticyclonic circulation around the Qingdao cold water mass, the vertical distributions of the Coriolis force, the total pressure gradient force, and the vertical friction force along the 35.5°N profile are shown (Fig. 6). In the surface layer (0–10 m), east of 121.75°E, the Coriolis force and vertical friction has high values, caused by the large current magnitude and strong wind. In the middle layer (10–30 m), the Coriolis force is positive west of 122°E when the total pressure gradient is negative, whereas the region east of 122°E shows the opposite behavior. However, west of 122°E, the Coriolis force is not identical to the total pressure gradient force, indicating that the vertical friction force cannot be ignored, which is consistent with the conclusion drawn from the horizontal momentum balance distribution. The Ekman ratio is the ratio of the friction and Coriolis terms and represents the relative significance of the friction force (Fig. 7). The Ekman ratio is usually high in coastal areas. Fig. 7 shows that the Ekman ratio is much greater along the bottom layer in the control run, which indicates that the friction term again plays a significant role around the Qingdao cold water mass. Most importantly, the geostrophic balance is not valid west of 122°E, where anticyclonic circulation exists.

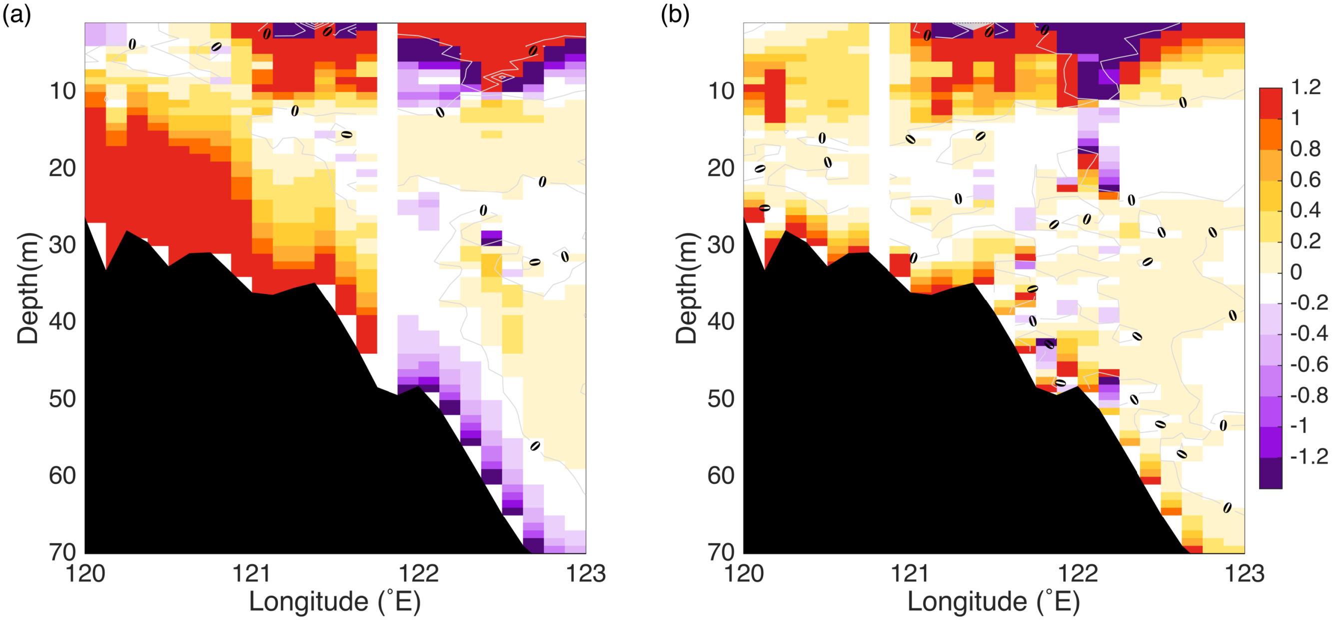

Figure 7. Vertical distributions of the Ekman ratio along the 35.5°N profile of the (a) control run and the (b) no-tide experiment in the zonal direction.

The geostrophic balance describes the equilibrium between the horizontal pressure gradient and Coriolis forces. Temperature and salinity distributions directly influence water density, altering the pressure gradient and affecting oceanic geostrophic currents. Near a Qingdao cold water mass, there are significant temperature and mild salinity gradients. However, owing to the lack of geostrophic balance, the density gradient caused by the temperature and salinity gradients associated with the Qingdao cold water mass is not the direct cause of the anticyclonic flow structure. This trend explains why, under the geostrophic balance, a cold center in the Northern Hemisphere would typically be associated with a cyclonic (counterclockwise) circulation, whereas the flow around the Qingdao cold water mass would exhibit a clockwise circulation pattern. The friction induced by tidal forcing disrupts the original geostrophic balance.

To some extent, the seasonal anticyclonic circulation is the dynamic reason for the Qingdao cold water mass. As mentioned in subsection 3.2, this type of anticyclonic structure prohibits heat transfer between the cold temperature center and the surrounding water column (Huang et al., 2019), but the seasonal anticyclonic circulation is not caused by the special temperature and salinity structure around the Qingdao cold water mass.

Since the geostrophic balance is not the direct reason for the circulation, other causes of the seasonal anticyclonic circulation around the Qingdao cold water mass should be identified. Tides play a significant role in the circulation processes of regional seas, contributing substantial amplitude, momentum, and energy flux. Early studies (B.H. Choi 1980; Byung Ho Choi, Eum, and Woo 2003; Moon, Hirose, and Yoon 2009; C. Xia et al. 2006) have shown that tidal characteristics in the Bohai and Yellow Seas are highly complex and play a significant role in local circulation and modulate dissipation, vertical mixing, and tidal energy. Owing to the large input of tidal energy and the combined effects of bottom friction related to shallow shelf topography, the dissipation of M_2 tidal energy (the principal lunar semidiurnal constituent) in shallow regions reaches 180 GW, accounting for approximately 11.1% of the global total (i.e., 2 TW). Additionally, the local seasonal monsoon may influence the structure of the anticyclonic circulation around the Qingdao cold water mass. Consequently, no-tide and no-wind simulations were conducted to analyze the impacts of tidal forcing and wind forcing on anticyclonic circulation.

3.5 Tidal Effects

In this subsection, the tidal effects on the seasonal anticyclonic circulation horizontally are discussed. The circulation pattern of the no-tide experiment in May at a depth of 25 m and the current deviations between the no-tide experiment and the control run (Fig. 8). Northward currents are present on the western side (to the west of 122°E) in the control run and the no-tide experiment, but the magnitudes are significantly greater in the no-tide experiment. At the center of the anticyclonic circulation, changes in the current are not evident. When the tidal forcing is turned off, the eastern side of the anticyclonic circulation direction reverses, changing from a southward current (in the control run, see Fig. 3b) to a northward current. The clockwise circulation pattern disappears in the no-tide experiment.

The momentum diagnostic of the no-tide experiments shows that the velocity decreases compared with that of the control run. When tidal forcing is not considered, the vertical friction along the bottom layer becomes much smaller than that in the control run. Without tidal forcing east of 122°E, the magnitude of the Coriolis terms increases (Fig. 9a), which is combined with a change in the circulation direction, indicating the significance of the tides around the anticyclonic circulation. In addition, the magnitude of the current in the entire region significantly increases, which is unrealistic, indicating that the dissipation and friction caused by tidal forcing are important for modulating circulation in anticyclonic areas.

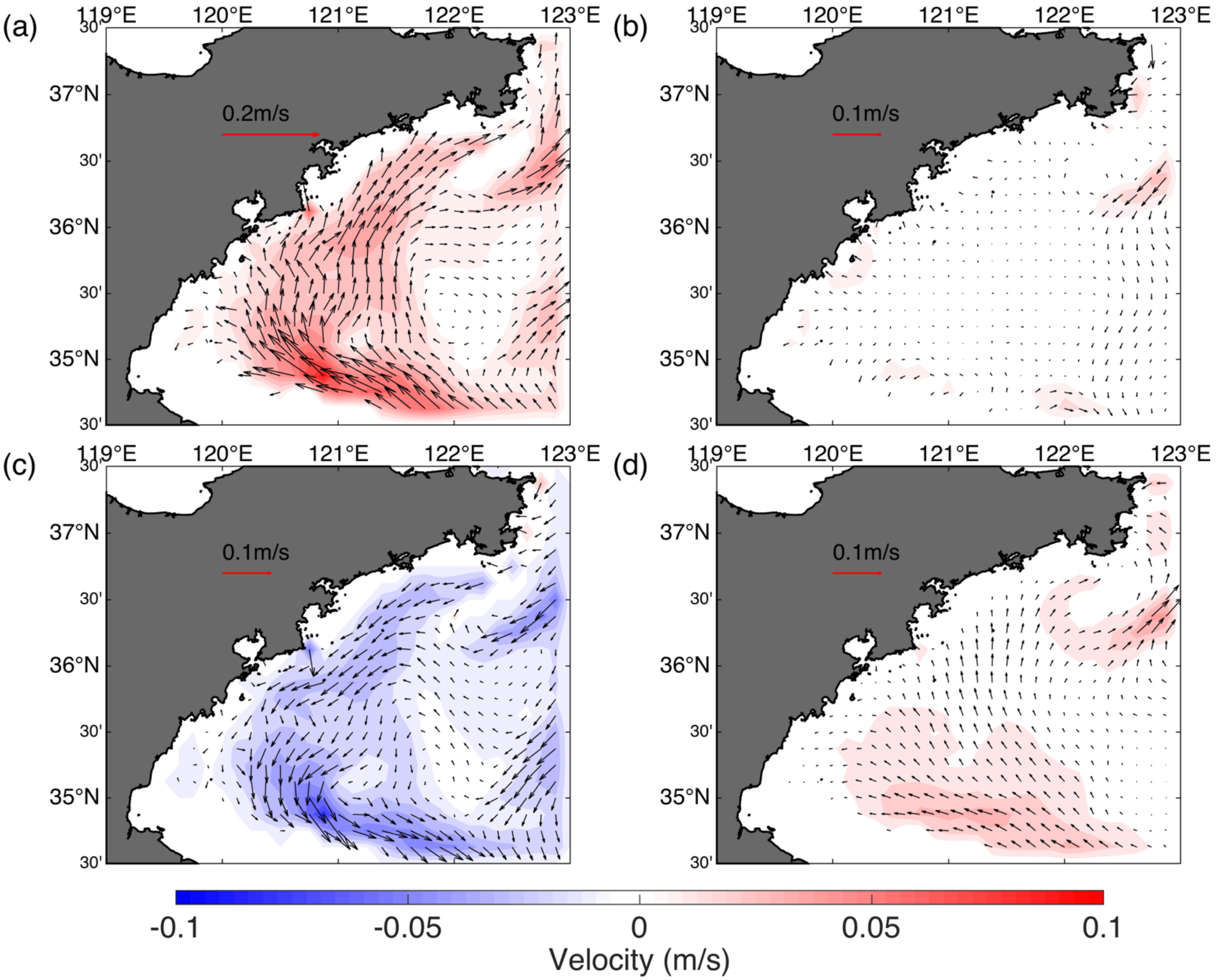

265 **Figure 8. Impacts of tidal forcing and wind forcings on anticyclonic circulation in May at 25 m (control run minus the no-wind experiment). (a) Circulation pattern of the no-tide experiment, (b) circulation pattern of the no-wind experiment, (c) difference between the no-tide experiment and control run, and (d) difference between the control run and the no-wind experiment.**

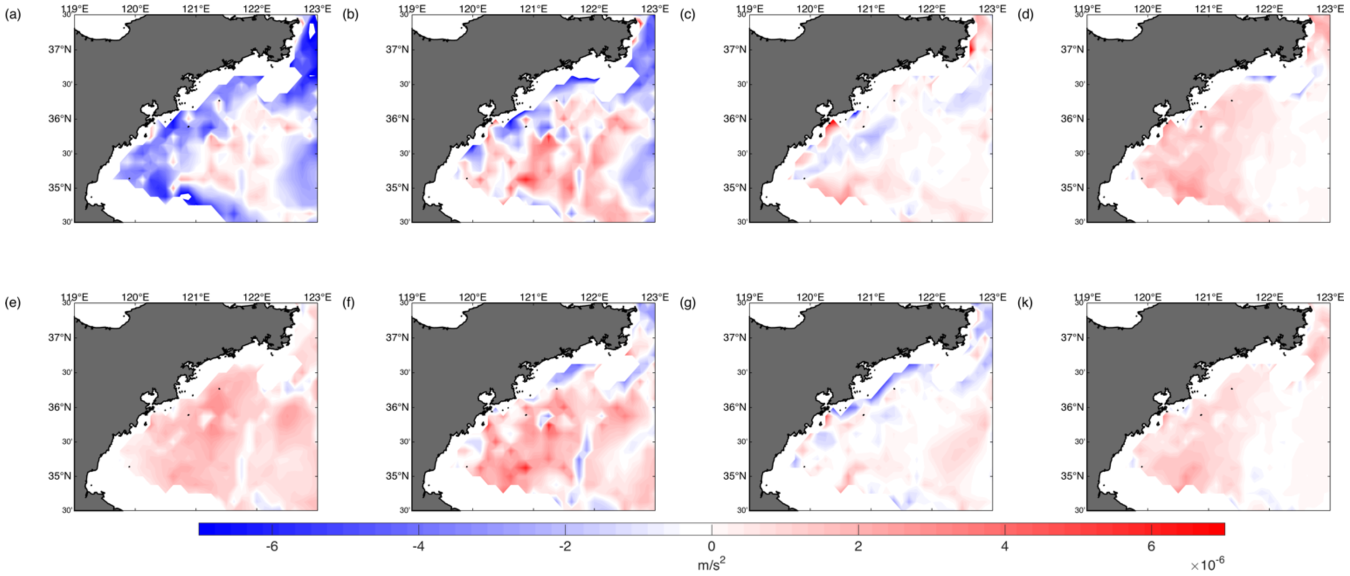

Figure 9. At 25 m, the momentum balance terms between the control run and the (a–d) no-tide experiment (control run minus no-tide experiment) and (e–k) between the control run and the no-wind experiment (control run minus no-wind experiment) are shown. (a, e) Coriolis force, (b, f) barotropic pressure gradient force, (c, g) baroclinic pressure gradient force, and (d, k) vertical friction term. The results are the monthly means for May.

3.6 Wind Effects

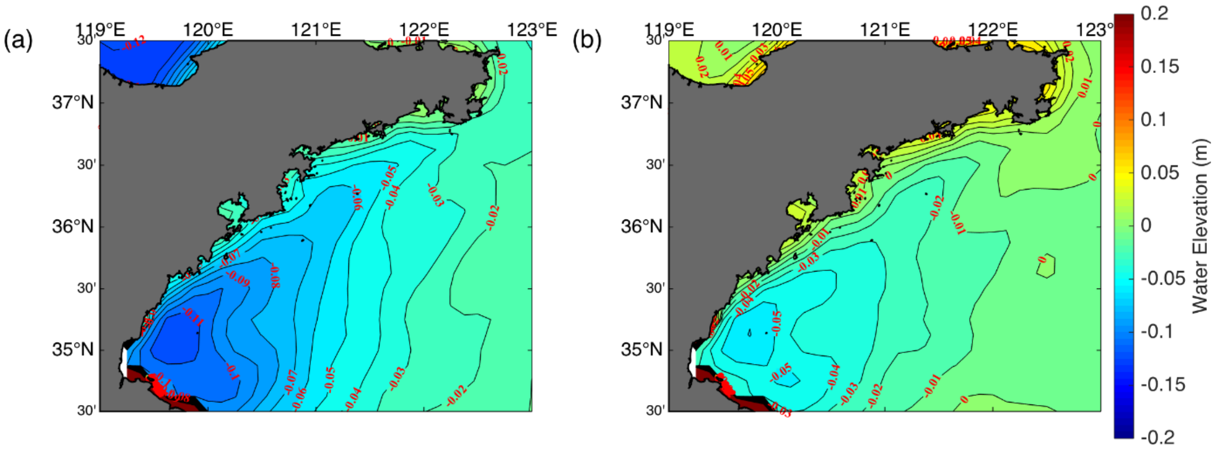

Figure 10. Surface elevation distributions of the (a) control run and (b) no-wind experiment. Monthly mean for May.

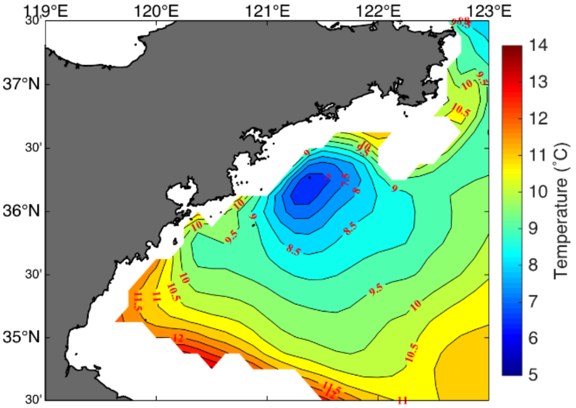

Figure 11. Horizontal temperature distribution at 25 m in the no-wind experiment (monthly mean for May).

Xu and Zhao (1999) demonstrated the effect of wind on the seasonal anticyclonic circulation around the Qingdao cold water mass using a two-dimensional numerical model, but a more thorough discussion is needed. Therefore, a no-wind experiment was conducted to examine the effect of wind on the seasonal anticyclonic circulation structure. The results show that wind is a dominant driving force for clockwise circulation. The general magnitude of the current weakens, particularly on the western side of the clockwise circulation (northward current), confirming again that the southerly wind along the Shandong Peninsula is the cause. In contrast, the influence of wind on the eastern side of the circulation is minor, as shown in Figs. 8b and 8d. The direction and magnitude of the eastern side are similar to those of the control run.

To compare the momentum changes and further analyze the wind forcing effect in this area, the difference in the momentum changes between the control run and the no-wind experiment was shown (control run minus the no-wind experiment, Figs. 9e–k). The Coriolis force decreases because of the weaker current when the wind forcing is turned off. The barotropic gradient force increases when the wind forcing is considered, indicating that the variation caused by water elevation increases with increasing wind forcing. With a southwesterly wind (Fig. A3), to the west of 121°E, the surface elevation is lower in the control run (Fig. 10). Accordingly, the barotropic pressure gradient force, which is the force exerted due to horizontal pressure differences caused by variations in sea surface height, also decreases when the wind forcing is turned off (Fig. 9g). In contrast, in the no-wind run, the temperature of the Qingdao cold water mass decreased by 2°C (Fig. 11) in the absence of mixing between the warm surface water and cold bottom water. These weaker mixing processes cause an increase in the baroclinic pressure gradient force in the area around the Qingdao cold water mass (120.5°-121.75°E, 35.5°-36.5°N) when the wind is eliminated. The vertical friction somewhat decreases because of the lack of wind stress in the no-wind experiment.

4. Discussion

4.1 Existence of Upwelling Near the Qingdao Cold Water Mass

Previous studies have investigated upwelling and the vertical secondary circulation in the Bohai and Yellow Seas and revealed that upwelling usually occurs in shallow areas along coasts, such as the Subei area and the region near the Korean Peninsula (Q. Wei et al. 2019; Lü et al. 2010). Lü et al. (2010) explained the tidal effect on upwelling, indicating that the front in the control run generates a relatively large baroclinic pressure gradient compared with when the tidal forcing is turned off, which further triggers distinct upwelling. In this work, we found that such an explanation can also explain the upwelling around the Qingdao cold water mass.

In this study, we also find that upwelling occurs from the surface layer to the bottom layer near the Qingdao cold water mass. Additionally, a refined analysis of the factors influencing upwelling around the Qingdao cold water mass has not yet been performed. Fig. 12a shows the vertical circulation structure in May at 35.625°N, which is around the horizontal center of the seasonal anticyclonic circulation. Upwellings occur near the frontal zones (122.375–122.5°E and 122.625–123°E) on the eastern and western sides of the Qingdao cold water mass, respectively. The seawater lifted by upwelling from the western and eastern sides of the cold pool converges toward the middle (122.5°E), making the vertical velocity surface layer at 122.5°E relatively small compared with that of the surrounding water.

We hypothesize that tidal forcing and wind forcing both contribute to upwelling around the Qingdao cold water mass. Wind forcings influence upwelling through Ekman transport. When tidal forcing is considered, the thermocline is reshaped, accompanied by changes in the baroclinic pressure gradient term, further strengthening the upwelling intensity on the east side. To test our hypothesis, we further analyzed the vertical circulation along the 35.625°N profile in May of the control run, the no-tide experiment, and the no-wind experiment (Fig. 12). Fig. 12 shows that in the control, an eastward flow occurs west of 122.50°E (red rectangle), and westward flow occurs east of 122.50°E (blue rectangle) above 25 m in the vertical direction. A comparison of Fig. 12a and 12c reveals that upwelling cycles occur in the red and blue rectangles in the control run. However, in the no-wind experiment (Fig. 12c), the magnitude of upwelling cycling significantly decreases. In the no-tide experiment (Fig. 12b), the magnitude of upwelling decreases as well, but mildly compared with no-wind experiment. The upwelling caused by the wind forcing can be explained by the Ekman theory because of the predominant southeasterly monsoon and the upwelling contributed by the tidal forcing. The following subsection explains the impact of tidal forcing on upwelling.

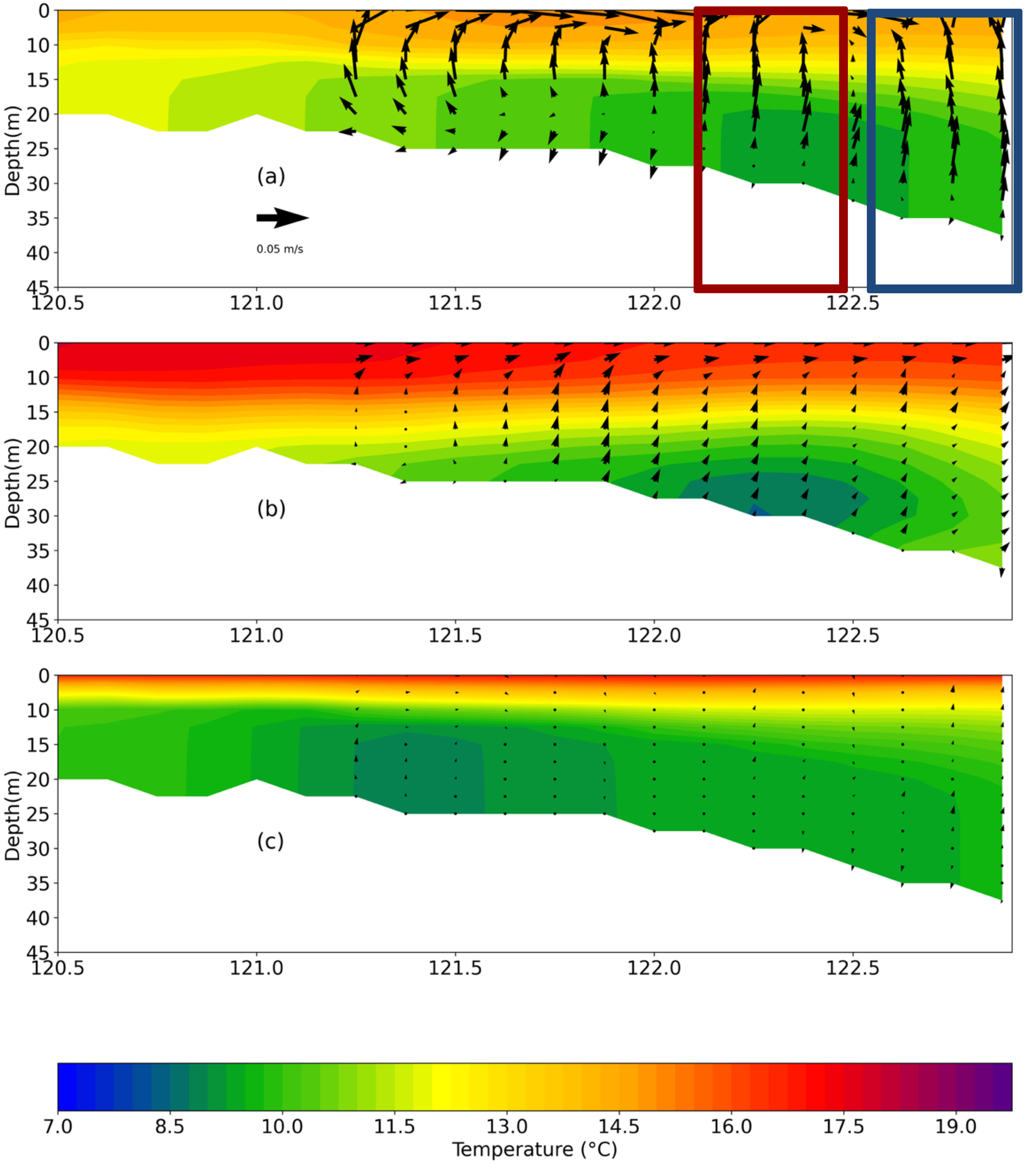

330 **Figure 12. Temperature (contours) and zonal–vertical current (arrows) along the 35.625°N profile in May in the ensemble means. For better visualization, the vertical velocity is multiplied by 1000 (unit: m/s). (a) Control run, (b) no-tide experiment, and (c) no-wind experiment. The red and blue boxes represent the frontal zones (122.375–122.5°E and 122.625–123°E) on the western and eastern sides of the Qingdao cold water mass.**

Tidal forcing plays a crucial role in shaping the characteristics of the thermocline, including the width of the front and the maximum temperature gradient. The front serves as a narrow transitional zone that separates stratified deep water from well-mixed shallow water, resulting in significant temperature (or density) differences across it. Owing to the mixing effects induced by tidal forces at the seafloor, isotherms near the bottom are predominantly orthogonal to the seabed topography at depths below 20 meters. Furthermore, in the control run, the front is both compressed and elevated. This study defines the front as the region where the magnitude of the horizontal and vertical temperature gradient ($\sqrt{\left(\frac{dT}{dx}\right)^2 + \left(\frac{dT}{dy}\right)^2}$) exceeds $1°C/m$. Under tidal forcing, the front is observed to exist within a depth range of approximately 2–20 m, whereas in the absence of tidal influences, the front extends from 2–25 m. A wider front correlates with a reduced intensity, indicating that the front is weaker in simulations without tidal effects. Additionally, the maximum vertical temperature gradient is greater in the control run ($1.78°C/m$) than in the no-tide simulation ($1.73°C/m$). Therefore, the front intensity decreases in the no-tide run, compared with the control run.

Variations in the front across regions create horizontal density differences, generating baroclinic pressure gradients. These gradients exert a horizontal force, driving denser water toward areas of lower density. Due to mass continuity, this horizontal movement results in upwelling. Fig. 13 shows the baroclinic pressure gradient force variation with depth at $35.625°N$, $122.25°E$ (within the red box in Fig. 13, representing the western portion) and $35.625°N, 122.75°E$ (within the blue box, representing the eastern portion). These two grid points are randomly selected within the red and blue boxes, and we have seen the grid points show similar trend. Generally, the magnitude of the baroclinic pressure gradient force is greater in the control run than in the no-tide run. The only exception is the baroclinic pressure gradient in the zonal direction at depths between 6 and 18 m. The baroclinic pressure gradient is greater in the no-tide run, which can be explained by the position shifting westward accompanied by thermocline position movement when the tidal forcing is turned off. The baroclinic pressure gradient force culminates at the bottom layer (approximately 30-m depth), but the strongest upwelling velocity occurs at a different location at depths above 25 m because the sea water's response to the baroclinic pressure gradient force takes time because of inertia. Additionally, other effects, such as wind forcings, can lead to the strongest upwelling velocity occurring at locations different from where the baroclinic pressure gradient force is at its maximum. To sum up, compared with the no-tide experiment, the front intensity increases in the no-tide run, which causes the baroclinic pressure gradients increase in most of the upwelling areas. The pressure gradient exerts a horizontal force. Due to mass continuity, the upwelling is triggered and enhanced when the tidal forcing is considered.

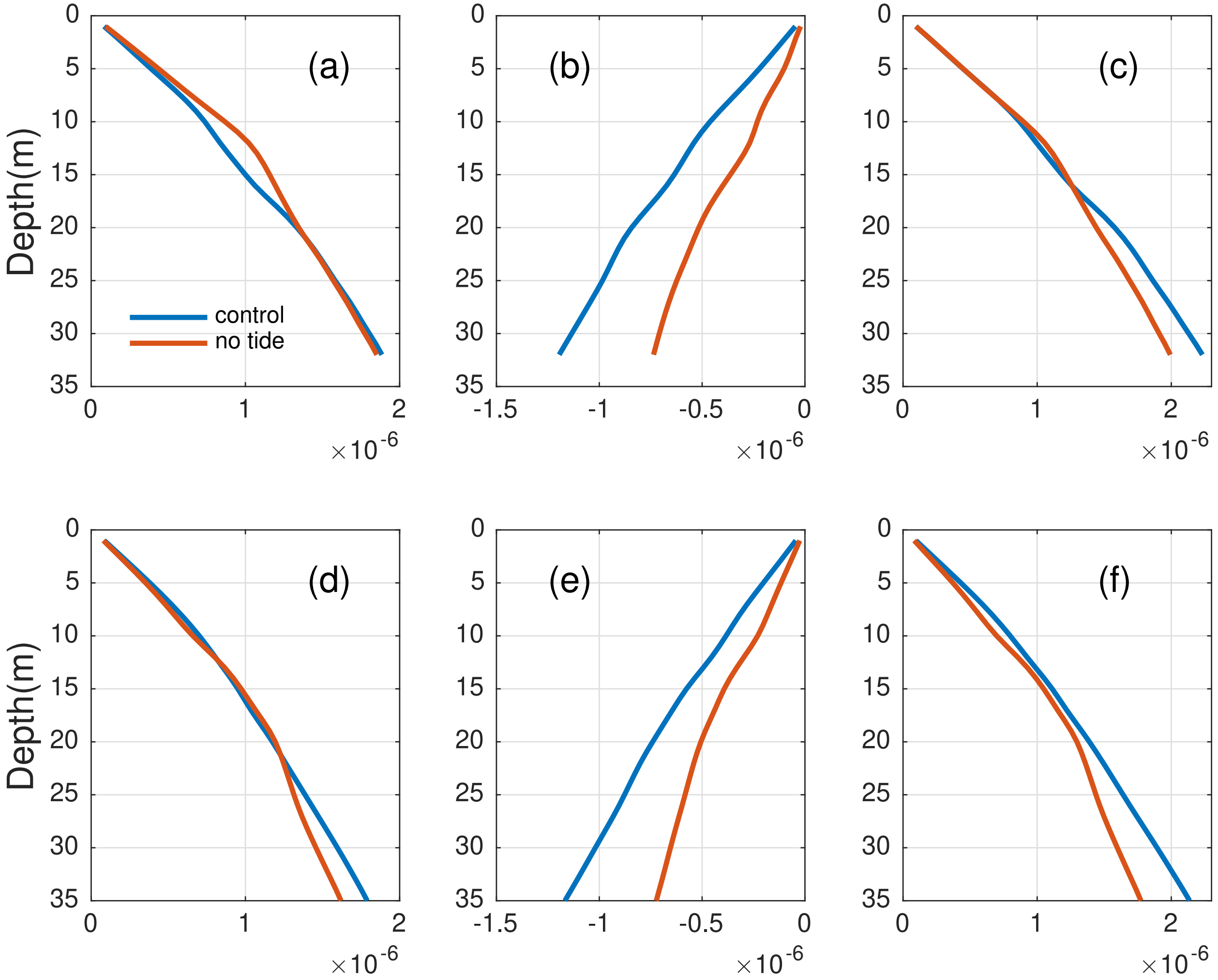

Figure 13. Baroclinic pressure gradient force in the (a–c) control run and (d–f) no-tide run. (a, d) Baroclinic pressure gradient force in the zonal direction, (b, e) baroclinic pressure gradient force in the meridional direction, and (c, f) magnitude of the baroclinic pressure gradient force.

4.2 Statistical Tests

As introduced in subsection 2.2, statistical tests have many applications in numerical climate simulations to separate and validate that the variation is caused by internal variability or changes in external forcing or parameterization (Conover 1999; Weisse, Heyen, and von Storch 2000; von Storch and Zwiers 1999; Livezey and Chen 1983; Zwiers and von Storch 1995). However, for the ocean regional simulation community, statistical tests are seldom applied.

In this study, a t-test was used to determine whether the differences between the ensemble means of the control run and the no-tide (no-wind run) may be caused by external forcings or can be explained by randomness. The results (Figs. 14 and 15) show the sensitivity of the formation of the spring cold water mass to the presence of tidal forcing and wind forcing. The grid points at which a t-test indicates that the effect of external forcing is significant are marked with a cross. Figs. 14 and 15 demonstrate that the difference between the control run and the no-tide ensemble (or the/no-wind ensemble) is significant, especially where the intraensemble deviations are large. The local percentages of local rejections are 51.29% and 89.68% for the no-wind and no-tide runs, respectively.

When such local tests are conducted, it is expected that even if the null hypothesis is valid, at approximately 5% of grid points, the null hypothesis is rejected (multiplicity of tests, cf. von Storch, and Zwiers, 1999). Since the rejection rate is itself a random variable, the false rejection rate can be much larger, but more than 20% is very unlikely. Here, the rate is considerably greater in both cases.

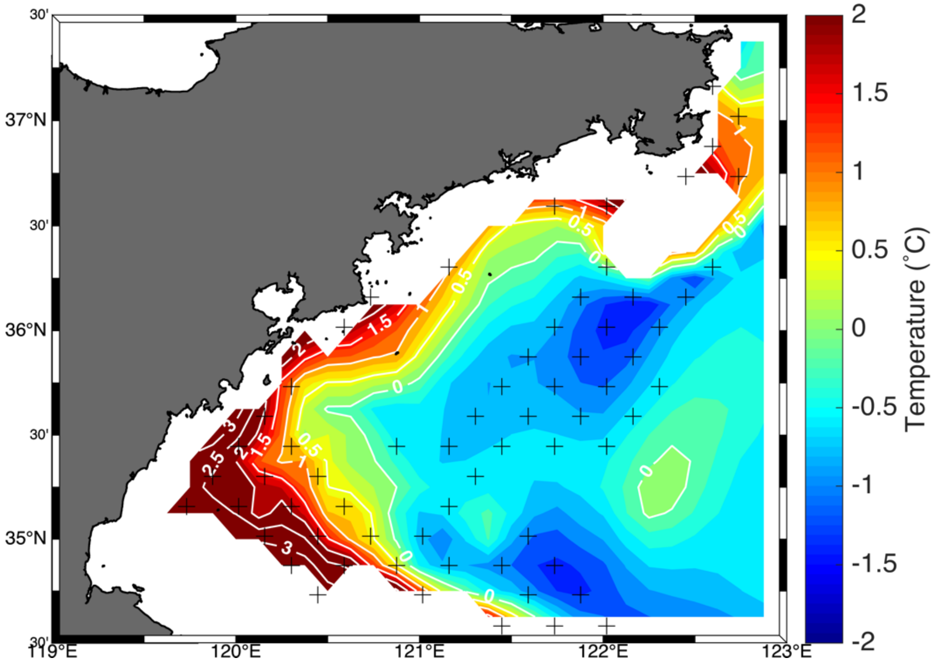

Figure 14. Temperature difference between the ensemble means of the control runs and the runs without tidal forcing. The crosses represent the areas where the difference between the control run and the run without tidal forcing was significant at the 5% level.

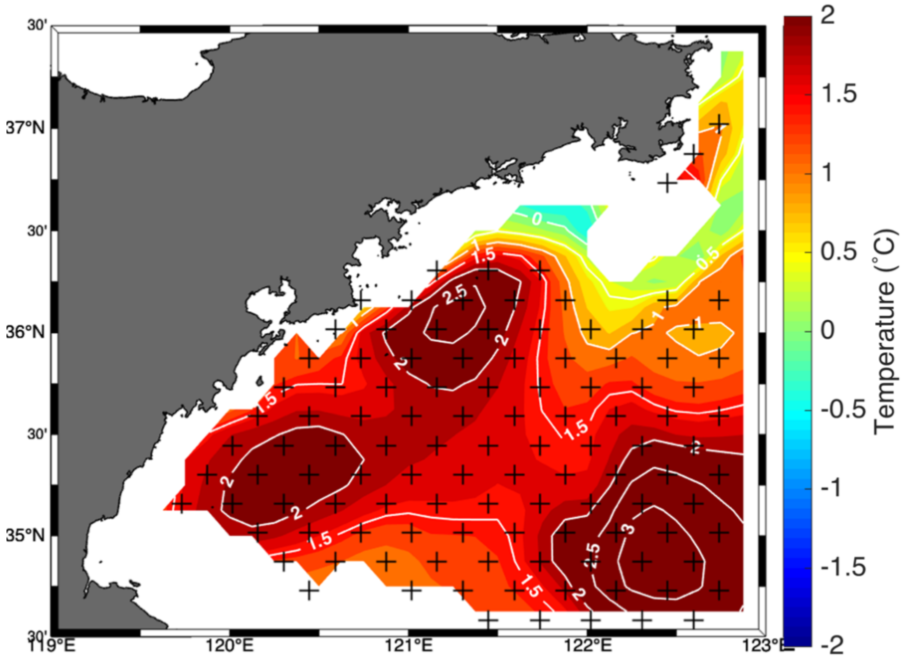

Figure 15. Temperature difference between the ensemble means of the control runs and the runs without wind forcings. The crosses represent the areas where the difference between the control run and the run without tidal forcing was significant at the 5% level.

4.3 Perspective and Implications of the Model Results

Previous studies have focused mainly on the seasonal variation in the formation of the Qingdao cold water mass and its mechanism (Ho et al. 1959; Q. Zhang et al. 2002; 2004; Yu et al. 2006; 2005; Zhang et al. 2016; Huang, Chen, and Lin 2019) but not the seasonal anticyclonic circulation around it. Some previous studies have reported an anticyclonic circulation around the Qingdao cold water mass (F. Zhang, Mao, and Leng 1987). The numerical results reveal that the northeastward current induced by the summer southwesterly winds interacts with the southward coastal current, leading to the formation of an anticyclonic circulation.

However, the link between the Qingdao cold water mass and the seasonal anticyclonic circulation has not been analyzed quantitatively. Based on the momentum balance, in this study, although there is a significant temperature gradient and a mild salinity gradient near the Qingdao cold water mass, the resulting density gradient from these temperature and salinity variations does not directly drive the observed anticyclonic flow structure, as the geostrophic balance is not maintained.

In addition to the insight gained regarding the dynamics of the Qingdao water mass, another innovative aspect of this paper is demonstrating how to separate random variations and signals in marginal seas caused by the experimental setup. The method was introduced in the climate sciences in 1974 (Chervin, Gates, and Schneider 1974), but it is rarely used when evaluating the results of numerical experiments in marginal seas.

Additionally, an ensemble simulation methodology has been applied in coastal ocean model simulations, which has rarely been applied and discussed in previous studies. Ensemble simulations can make the conclusion more robust and exclude the random phenomenon in a single simulation maximally.

4.4 Limitations of the study

In this study, the 2019 model results were used as an example. Huang et al. reported similar basic characteristics of the temperature and salinity of the Qingdao cold water mass in 2010 (2019). This study is limited to the 2019 simulation. Future work would investigate the interannual variation characteristics and mechanisms of the interannual variation in this anticyclonic circulation.

Also, this study focused on submesoscale horizontal and vertical circulation around the Qingdao cold water mass, and further exploration of boundary layer theories is worthwhile since topography and bottom friction play a role in the coastal area. Future analyses will investigate the boundary layer variation caused by tidal forcing.

5. Conclusions

Based on numerical models, the main characteristics and related dynamic processes of the local seasonal anticyclonic circulation around the Qingdao cold water mass during spring and summer were analyzed in this study. The Qingdao cold water mass emerges in April and is fully developed in May, combined with a seasonal anticyclonic circulation. Two major scientific questions mentioned in the introduction are answered: (1) The Qingdao cold water mass is not the direct reason for the seasonal anticyclonic circulation around the Qingdao cold water mass. (2) Both tidal forcing and wind forcings play roles in horizontal anticyclonic circulation. When wind forcing is not considered, the current's general magnitude weakens, particularly on the western side of the seasonal anticyclonic circulation (northward current), confirming again that the southeasterly wind along the Shandong Peninsula is the cause of the northward current on the west side of the Qingdao cold water mass. Additionally, when tidal forcing is not considered, the eastern side of the seasonal anticyclonic circulation direction reverses, changing from a southward current to a northward current. Vertically, the tidal front causes a baroclinic pressure gradient force, further triggering upwelling; wind forcing contributes to Ekman upwelling.

Author contributions. LL formulated all the simulations, analyzed the results, and wrote the manuscript. HvS provided guidance and wrote and revised the manuscript, particularly the statistical test portion. DY helped with the numerical model momentum balance output and provided guidance in drafting and revising the manuscript.

Competing interests. The contact author has declared that none of the authors has any competing interests.

Acknowledgments. We are grateful to the German Climate Computer Center (DKRZ) for providing computer resources. Yang Ding was supported by the National Natural Science Foundation (NSFC, No. 42130403 and 42076010).

Data availability. The datasets generated during and/or analyzed during the current study are available from the corresponding author upon reasonable request.

References

Chen, Changsheng, Roberet Beardsley, and Geoffrey Cowles. 2006. “An Unstructured Grid, Finite-Volume Coastal Ocean Model (FVCOM) System.” Oceanography 19 (1): 78–89. https://doi.org/10.5670/oceanog.2006.92.

Chen, Changsheng, Hedong Liu, and Robert C. Beardsley. 2003. “An Unstructured Grid, Finite-Volume, Three-Dimensional, Primitive Equations Ocean Model: Application to Coastal Ocean and Estuaries.” Journal of Atmospheric and Oceanic Technology 20 (1): 159–86. https://doi.org/10.1175/1520-0426(2003)020<0159:AUGFVT>2.0.CO;2.

Chervin, Robert M., W. Lawrence Gates, and Stephen H. Schneider. 1974. “The Effect of Time Averaging on the Noise Level of Climatological Statistics Generated by Atmospheric General Circulation Models.” Journal of the Atmospheric Sciences 31 (8): 2216–19. https://doi.org/10.1175/1520-0469(1974)031<2216:TEOTAO>2.0.CO;2.

Choi, B.H. 1980. A Tidal Model of the Yellow Sea and the Eastern China Sea. KORDI Report. Korea Ocean Research and Development Institute. https://books.google.de/books?id=nQwIAQAAIAAJ.

Choi, Byung Ho, Hyun Min Eum, and Seung Buhm Woo. 2003. “A Synchronously Coupled Tide–Wave–Surge Model of the Yellow Sea.” Coastal Engineering 47 (4): 381–98. https://doi.org/10.1016/S0378-3839(02)00143-6.

Conover, W. J. 1999. Practical Nonparametric Statistics. 3rd ed. Wiley Series in Probability and Statistics. Applied Probability and Statistics Section. New York: Wiley.

Diao, Xinyuan. 2015. “The study of Yellow Sea Warm Current, Yellow Sea Cold Water Mass and their evolution process in sping.” Qingdao: Institute of Oceanology, Chinese Academy of Sciences.

Egbert, Gary D., and Svetlana Y. Erofeeva. 2002. “Efficient Inverse Modeling of Barotropic Ocean Tides.” Journal of Atmospheric and Oceanic Technology 19 (2): 183–204. https://doi.org/10.1175/1520-0426(2002)019<0183:EIMOBO>2.0.CO;2.

Ho, Chung-pen, Yuan-xiang Wang, Zong-you Lei, and Si Xu. 1959. “A Prelimenary Study of the Formation of Yellow Sea Cold Mass and Its Properties.” Oceanologia Et Limnologia Sinica 2 (1): 11—15.

Huang, Hao, Xueen Chen, and Lin Lin. 2019. “Evolution and Mechnism of the Qingdao Cold Water Mass.” Oceanologia Et Limnologia Sinica 50 (6): 1191–1200.

Hur, H.B., G.A. Jacobs, and W.J. Teague. 2000. “Monthly Variations of Water Masses in the Yellow and East China Seas.” Journal of Oceanography 56 (3): 359.

Lin, Lin, Hans von Storch, Donglin Guo, Shengquan Tang, Peng Zheng, and Xueen Chen. 2022. “The Effect of Tides on Internal Variability in the Bohai and Yellow Sea.” Dynamics of Atmospheres and Oceans 98 (June):101301. https://doi.org/10.1016/j.dynatmoce.2022.101301.

Lin, Lin, Hans von Storch, Xueen Chen, Wensheng Jiang, and Shengquan Tang. 2023. “Link between the Internal Variability and the Baroclinic Instability in the Bohai and Yellow Sea.” Ocean Dynamics 73 (12): 793–806. https://doi.org/10.1007/s10236-023-01583-7.

Liu, G.M., H. Wang, S. Sun, and B.P. Han. 2003. “Numerical Study on Density Residual Currents of the Bohai Sea in Summer.” Chin. J. Oceanol. Limnol. 21 (2): 106–13.

Livezey, Robert E., and W. Y. Chen. 1983. “Statistical Field Significance and Its Determination by Monte Carlo Techniques.” Monthly Weather Review 111 (1): 46–59. https://doi.org/10.1175/1520-0493(1983)111<0046:SFSAID>2.0.CO;2.

Lü, Xingang, Fangli Qiao, Changshui Xia, Guansuo Wang, and Yeli Yuan. 2010. “Upwelling and Surface Cold Patches in the Yellow Sea in Summer: Effects of Tidal Mixing on the Vertical Circulation.” Continental Shelf Research 30 (6): 620–32. https://doi.org/10.1016/j.csr.2009.09.002.

Mellor, George L., and Tetsuji Yamada. 1982. “Development of a Turbulence Closure Model for Geophysical Fluid Problems.” Reviews of Geophysics 20 (4): 851. https://doi.org/10.1029/RG020i004p00851.

Moon, Jae-Hong, Naoki Hirose, and Jong-Hwan Yoon. 2009. “Comparison of Wind and Tidal Contributions to Seasonal Circulation of the Yellow Sea.” Journal of Geophysical Research 114 (C8): C08016. https://doi.org/10.1029/2009JC005314.

Penduff, Thierry, William Llovel, Sally Close, Ixetl Garcia-Gomez, and Stéphanie Leroux. 2019. “Trends of Coastal Sea Level Between 1993 and 2015: Imprints of Atmospheric Forcing and Oceanic Chaos.” Surveys in Geophysics 40 (6): 1543–62. https://doi.org/10.1007/s10712-019-09571-7.

Saha, Suranjana, Shrinivas Moorthi, Xingren Wu, Jiande Wang, Sudhir Nadiga, Patrick Tripp, David Behringer, et al. 2014. “The NCEP Climate Forecast System Version 2.” Journal of Climate 27 (6): 2185–2208. https://doi.org/10.1175/JCLI-D-12-00823.1.

Von Storch, Hans, and Francis W. Zwiers. 1999. Statistical Analysis in Climate Research. Cambridge ; New York: Cambridge University Press.

Tang, Shengquan, Hans von Storch, and Xueen Chen. 2020. “Atmospherically Forced Regional Ocean Simulations of the South China Sea: Scale Dependency of the Signal-to-Noise Ratio.” Journal of Physical Oceanography 50 (1): 133–44. https://doi.org/10.1175/JPO-D-19-0144.1.

Wan, X.G., Xianwen Bao, Dexing Wu, and H Jiang. 2004. “Numerical Diagnostic Simulation of Summertime Tide-Induced, Wind-Driven and Thermohaline Currents in the Bohai Sea.” Oceanologia Et Limnologia Sinica 35 (1): 47–53.

Wang, Bin, Naoki Hirose, Boonsoon Kang, and Katsumi Takayama. 2014. “Seasonal Migration of the Yellow Sea Bottom Cold Water.” Journal of Geophysical Research: Oceans 119 (7): 4430–43. https://doi.org/10.1002/2014JC009873.

Wei, Hao, Jie Shi, Youyu Lu, and Yuan Peng. 2010. “Interannual and Long-Term Hydrographic Changes in the Yellow Sea during 1977–1998.” Deep Sea Research Part II: Topical Studies in Oceanography 57 (11–12): 1025–34. https://doi.org/10.1016/j.dsr2.2010.02.004.

Wei, Qinsheng, Baodong Wang, Qingzhen Yao, Zhigang Yu, Mingzhu Fu, Junchuan Sun, Bochao Xu, Linping Xie, and Ming Xin. 2019. “Physical-Biogeochemical Interactions and Potential Effects on Phytoplankton and Ulva Prolifera in the Coastal Waters off Qingdao (Yellow Sea, China).” Acta Oceanologica Sinica 38 (2): 11–23. https://doi.org/10.1007/s13131-019-1344-3.

Weisse, Ralf, Hauke Heyen, and Hans von Storch. 2000. “Sensitivity of a Regional Atmospheric Model to a Sea State–Dependent Roughness and the Need for Ensemble Calculations.” Monthly Weather Review 128 (10): 3631–42. https://doi.org/10.1175/1520-0493(2000)128<3631:SOARAM>2.0.CO;2.

Xia, Changshui, Fangli Qiao, Yongzeng Yang, Jian Ma, and Yeli Yuan. 2006. “Three-Dimensional Structure of the Summertime Circulation in the Yellow Sea from a Wave-Tide-Circulation Coupled Model.” Journal of Geophysical Research 111 (C11): C11S03. https://doi.org/10.1029/2005JC003218.

Xia, Ju, and Xuejun Xiong. 2013. “Distributions and Seasonal Changes of Water Temperature in the Bohai Sea, Yellow Sea and East China Sea.” Advances in Marine Science 31 (1): 55–68.

Xu, Danya, and Baoren Zhao. 1999. “Existential proof and numerical study of a mesoscale anticyclonis eddy in the Qingdao-Shidao offshore.” Acta Oceanologica Sinica, no. 2, 18–26.

Yu, Fei, Zhi-xin Zhang, Xin-yuan Diao, Jing-song Guo, and Yuan-xiang Tang. 2006. “Analysis of Evolution of the Huanghai Sea Cold Water Mass and Its Relationship with Adjacent Water Masses.” Acta Oceanologica Sinica 05:26–34. https://doi.org/CNKI:SUN:SEAC.0.2006-05-002.

Yu, Fei, Zhang Zhixin, Xinyuan Diao, Jingsong Guo, and Rengfeng Ge. 2005. “Analysis of Water Temperature Distribution Characteristics in the Southern Yellow Sea in Spring.” Advances in Marine Science 23 (3): 281–88.

Yuan, Dongliang, Yao Li, Fangli Qiao, and Wei Zhao. 2013. “Temperature Inversion in the Huanghai Sea Bottom Cold Water in Summer.” Acta Oceanologica Sinica 32 (3): 42–47. https://doi.org/10.1007/s13131-013-0287-3.

Zhang, cunyi. 1986. “Analysis of the Strength and Yearly Vairations of Qingdao Cold Water-Masses.” Marine Sciences 10 (3): 48–51.

Zhang, Fagao, Hanli Mao, and Yangui Leng. 1987. “Analysis of Drift Bottle and Drift Card Experiments in Bohai Sea and Huanghai Sea (1975–80).” Chinese Journal of Oceanology and Limnology 5 (1): 67–72. https://doi.org/10.1007/BF02848524.

Zhang, Qilong, Yijun Hou, Minghua Cheng, Xingquan Liu, and Baoshu Yin. 2004. “Variation Features in Qingdao Cold Water Mass Strength.” Studia Marina Sinica 46 (1): 13–21.

Zhang, Qilong, Xingquan Liu, Minghua Cheng, and Xinsheng Y. 2002. “Characteristics and Formation Causes of Qingdao Cold Water Mass.” Chinese Journal of Oceanology and Limnology 20:303–8.

Zhang, Qilong, Yuling Yang, and Minghua Cheng. 1994. “An Analysis of Characteristics of Thermohaline Structures in the South Yellow Sea in Spring.” Haiyang Xuebao 18 (6): 50–55.

Zhang, Yuankui, and Xiaotong Geng. 1989. Relationship between Fishery and Hydrological Situation. Hydrological regime in Shandong coastal waters. Ji-nan:Shandong Map Press.

Zheng, Dong, and Ruian Zhang. 1983. “Analysis of Spring Water Masses in the Sea Area off Yantai, Weihai, and Shidao.” Marine Science Bulletin 01:61–68.

Zhou, Feng, Daji Huang, Huijie Xue, Jiliang Xuan, Tao Yan, Xiaobo Ni, Dingyong Zeng, and Jia Li. 2017. “Circulations Associated with Cold Pools in the Bohai Sea on the Chinese Continental Shelf.” Continental Shelf Research 137 (April):25–38. https://doi.org/10.1016/j.csr.2017.02.005.

Zhu, Ping, and Hui Wu. 2018. “Origins and Transports of the Low-Salinity Coastal Water in the Southwestern Yellow Sea.” Acta Oceanologica Sinica 37 (4): 1–11. https://doi.org/10.1007/s13131-018-1200-x.

Zwiers, Francis W., and Hans von Storch. 1995. “Taking Serial Correlation into Account in Tests of the Mean.” Journal of Climate 8 (2): 336–51. https://doi.org/10.1175/1520-0442(1995)008<0336:TSCIAI>2.0.CO;2.

Zhang, Qilong, Zhi-Liang Liu, Jifeng Qi, Dezhou Yang, and Dongmei Zheng. 2016. “Study on the Mechanism of the Dissipation of the Qingdao Cold Water Mass.” Acta Oceanologica Sinica 38 (5): 27–33.

Huang, Hao, Xue'en Chen, and Lin Lin. 2019. “Research on the Formation and Evolution of the Qingdao Cold Water Mass.” Oceanologia et Limnologia Sinica 50 (6): 1191–1200.

Appendix

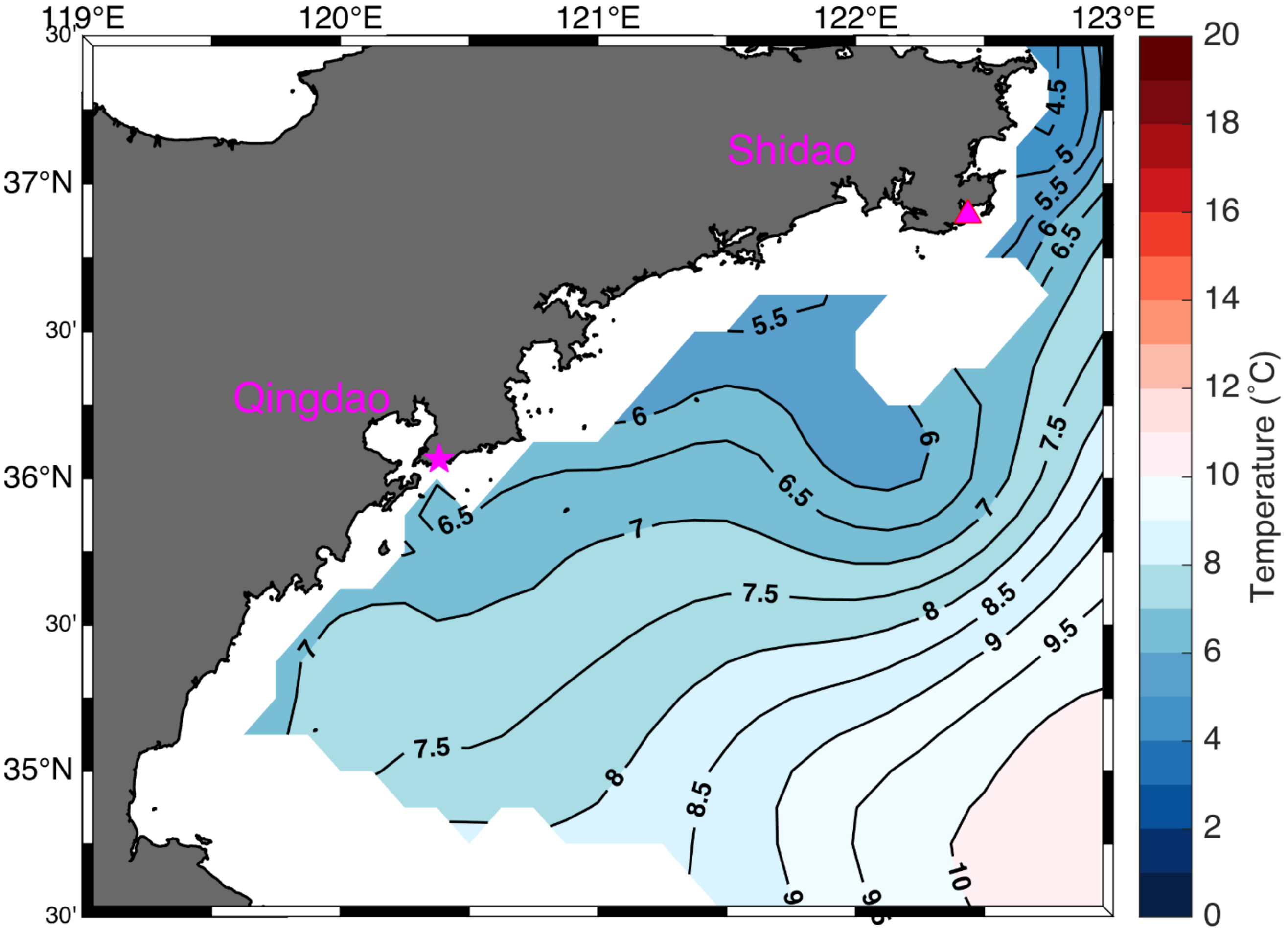

Figure A1. Monthly mean temperature evolution of the Qingdao cold water mass in March at a depth of 25 m, as derived from the ensemble mean of the control runs.

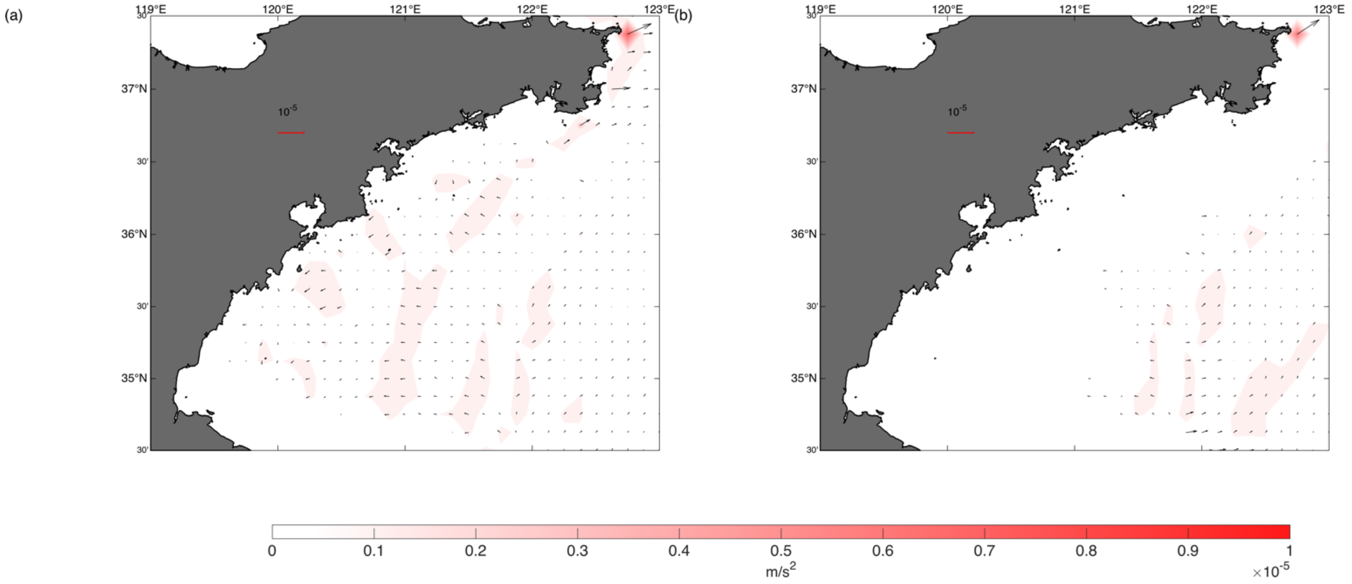

Figure A2. Horizontal distributions of the sum of the barotropic gradient force $-g\frac{\partial\zeta}{\partial x}$, baroclinic pressure gradient force $-\frac{1}{\rho}\frac{\partial}{\partial x}\int_z^\zeta \rho g dz$, Coriolis force fv and vertical friction force F_u (monthly mean for May) at depths of (a) 25 and (b) 40 m.

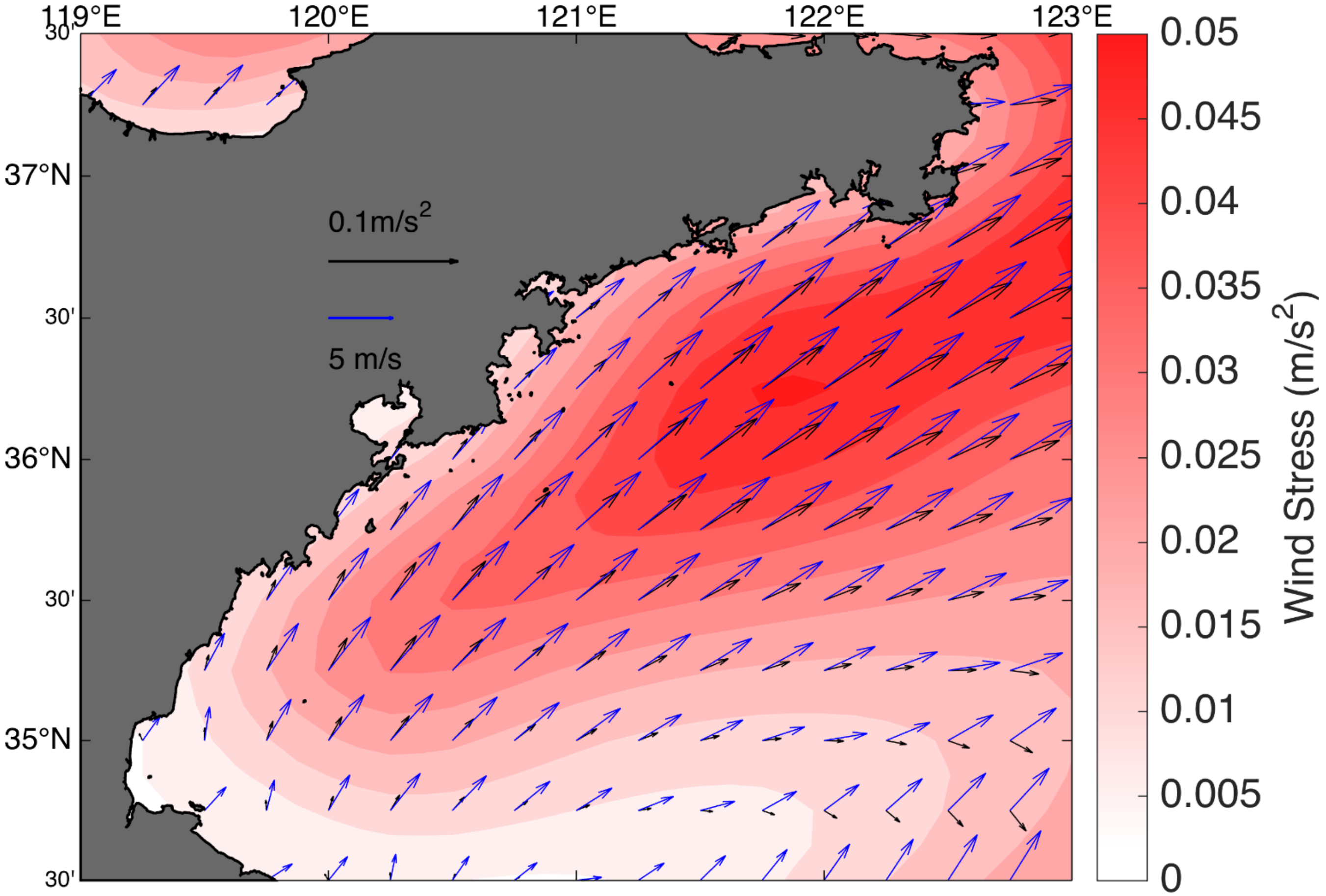

Figure A3. Mean surface wind stress in May 2019 used in the control run and the no-tide ensembles. (The magnitudes of the wind stress and wind are different. To show both in the same diagram, two scales were used. The blue and black arrows represent the magnitudes of the wind stress and wind, respectively.)